Nanoscale Advances

PAPER

View Article Online
View Journal | View Issue

Check for updates

Cite this: *Nanoscale Adv.*, 2025, 7, 2248

An ultra-violet and infrared dual-band photodetector using a Ga_2O_3 thin film and HgTe colloidal quantum dots†

Qiqi Zheng,[a] Yu Yang,[b] Liansheng Li,[b] Qing-An Xu,[b] Kenan Zhang,[c] Xiaomeng Xue,[a] Lisha Ma,[a] Jianhao Yu,[d] Wanjun Li*[d] and Menglu Chen *[ace]

Received 25th November 2024
Accepted 14th February 2025

DOI: 10.1039/d4na00978a

rsc.li/nanoscale-advances

Dual-band photodetection of ultraviolet (UV) and infrared (IR) light is an advanced technology aimed at simultaneously or selectively detecting signals from these two distinct wavelength bands. This technique offers broad application prospects, particularly in environments requiring multispectral information. In this work, a solar-blind UV photodetector made from an amorphous Ga_2O_3 (a-Ga_2O_3) thin film was combined with a short-wave infrared photodetector made from a HgTe colloidal quantum dot (CQD) film. The photodetector exhibited a high responsivity of up to 1808 A W^{-1}, detectivity of 3.88×10^{14} Jones, and an external quantum efficiency of 8.8×10^5% at UV wavelength as well as a responsivity of 0.25 A W^{-1}, detectivity of 1.45×10^{10} Jones, and an external quantum efficiency of 15.5% at short-wave infrared wavelength. Furthermore, corona discharge detection using this photodetector was demonstrated.

1. Introduction

Dual-band optoelectronic devices that operate in the ultraviolet (UV) and infrared (IR) regions are critical for civilian and military applications such as solar cells,[1] fire flame detection,[2] corona detection,[3] communications, and missile interception.[4] UV-IR dual-band detectors can respond to corresponding bands simultaneously, which enhances target recognition and lowers false alarm rates.[5]

For UV photodetection, ultra-wide bandgap semiconductor materials are being investigated. Currently, diamond,[6] AlGaN,[7] MgZnO,[8] and Ga_2O_3 (ref. 9) are the widely used materials for ultrawide bandgap semiconductors. Among them, Ga_2O_3 has a direct bandgap of 4.5–5.2 eV and an absorption cut-off wavelength of less than 280 nm,[10] and the corresponding PD has a very low background noise with a good signal-to-noise ratio and low error rate.[11] Furthermore, it has very high breakdown field strength values of up to 8 MV cm^{-1},[12] good transparency, and great thermal and chemical stability and is better suited for dual-band integration.[13,14] Recently, He *et al.*[15] realized MOCVD heteroepitaxial β-Ga_2O_3 and black phosphorus (BP) heterojunction solar-blind UV and IR dual-band photodetectors with considerable optical response in the respective bands. Chen *et al.*[16] employed a p-type BP coupled with silicon-doped β-Ga_2O_3 to manufacture a dual-band junction field-effect phototransistor (JFEPT), which is an essential reference for the realization of high-performance UV-IR dual-band detectors. However, large-scale fabrication is still a challenge in photodetection using 2D materials.

Colloidal quantum dots (CQDs),[17] as a promising material for the development of high-performance broadband photoconductive devices, provide a good platform for infrared technology owing to their tunable band gap and easy solution processing.[18,19] Among others, HgTe CQDs have demonstrated the widest spectral tunability so far from the shortwave infrared (SWIR) to the terahertz region[20,21] and have been widely used in dual-band PD preparation owing to their high integration, high photoelectric conversion efficiency, and fast response.[22] Zhang *et al.*[23] created a CMOS multispectral imager with spectral response from the ultraviolet and visible to the SWIR region, resulting in high-resolution monochromatic and merged multispectral images, and He *et al.*[3] developed a combination of ultrasonic, infrared, and ultraviolet portable on-line partial discharge detection system using image alignment and fusion techniques, which has a wide range of applications in the early detection of power equipment problems.

In this work, we parallelly combined Ga_2O_3 and HgTe CQD thin films on interdigital electrodes to create dual-band photodetectors and investigated their optoelectronic

[a] *School of Optics and Photonics, Beijing Institute of Technology, Beijing 100081, China. E-mail: menglu@bit.edu.cn*

[b] *Optoelectronic Measurement and Intelligent Perception Zhongguancun Open Lab, Beijing 100190, China*

[c] *Zhejiang Key Laboratory of 3D Micro/Nano Fabrication and Characterization, Westlake Institute for Optoelectronics, Zhejiang 311421, China*

[d] *College of Physics and Electronic Engineering, Chongqing Normal University, Chongqing 401331, China. E-mail: liwj@cqnu.edu.cn*

[e] *National Key Laboratory of Materials for Integrated Circuits, Shanghai Institute of Microsystem and Information Technology, Chinese Academy of Sciences, Shanghai, 200050, China*

† Electronic supplementary information (ESI) available. See DOI: https://doi.org/10.1039/d4na00978a

characteristics. The a-Ga_2O_3 solar-blind photodetector (SBPD) was prepared by sequentially sputtering the Ga_2O_3 film and ITO electrodes using RF magnetron sputtering at room temperature, which exhibited a high responsivity of 1808 A W^{-1}, detectivity of 3.88×10^{14} Jones, and external quantum efficiency of 8.8×10^5%. The HgTe CQD was then spin-coated on ITO electrodes, which showed a responsivity of 0.25 A W^{-1}, detectivity of 1.45×10^{10} Jones, and external quantum efficiency of 15.5%. Furthermore, the capability of this dual-band coupled photodetector to detect corona discharge was investigated.

2. Experimental section

2.1 a-Ga_2O_3 SBPD

First, amorphous Ga_2O_3 thin films were deposited on (0001) sapphire (c-Al_2O_3) substrates *via* RF magnetron sputtering at room temperature. The Ga_2O_3 material is a commercial ceramic target with a purity of 4 N (99.99%). Prior to sputtering, the chamber background pressure was 5×10^{-4} Pa and the high-purity Ar (99.99%) flow rate was 40 sccm. During sputtering, the vacuum was maintained at 1.0 Pa, and the power and time of sputtering were 150 W and 1.5 h, respectively. Subsequently, a simple mask process combined with RF magnetron sputtering was performed to deposit indium tin oxide (ITO) transparent electrodes under an Ar_2 atmosphere and with a power of 120 W for 10 minutes. The effective photosensitive area of the devices was 0.00234 cm^2, with electrode dimensions of 30 μm (spacing and width) and 1 mm (length).

2.2 HgTe CQD photoconductor

HgTe CQD synthesis. 108.8 mg of $HgCl_2$ salt was dissolved in 16 mL oleylamine and heated at 100 °C for 1 h until complete dissolution, and the reaction temperature was adjusted to 64 °C. 400 μL (0.4 mmol) of TOPTe was injected and reacted for 5 min to obtain 2 μm CQD.

Preparation of single-pixel devices. HgTe CQD devices are prepared by spin-coating the CQD on the sapphire substrates with interdigital electrodes. Each layer is treated with an EDT/HCl/IPA solution (1 : 1 : 50 by volume) for 10 s, rinsed with IPA, and dried. The effective device area is 0.5 mm^2, where the 50 pairs of interdigitated electrodes have a finger width of 10 μm, a gap of 10 μm, and a finger length of 1 mm.

2.3 Material and device characterization

Material characterization. The absorption spectrum is obtained using a Fourier Transform Infrared spectrometer (FTIR) and an N4S UV-Vis spectrophotometer. The a-Ga_2O_3 and HgTe CQD thin films were analysed using a Bruker D8 Advance XRD system, employing Cu Kα1 radiation ($\lambda = 1.540598$ nm).

Device characterization. Electrical properties of devices, including voltammetric (*I–V*) characteristic curves and transient response (*I–t*) curves, were assessed using a Keithley 2450 and Keithley 2602 B source meter. A xenon lamp emitting at 254 nm served as the deep ultraviolet light source. A 600 °C blackbody radiation source was used as the IR light source. Additionally, an arc simulator was employed to mimic a corona source in high voltage discharge experiments for testing the devices at

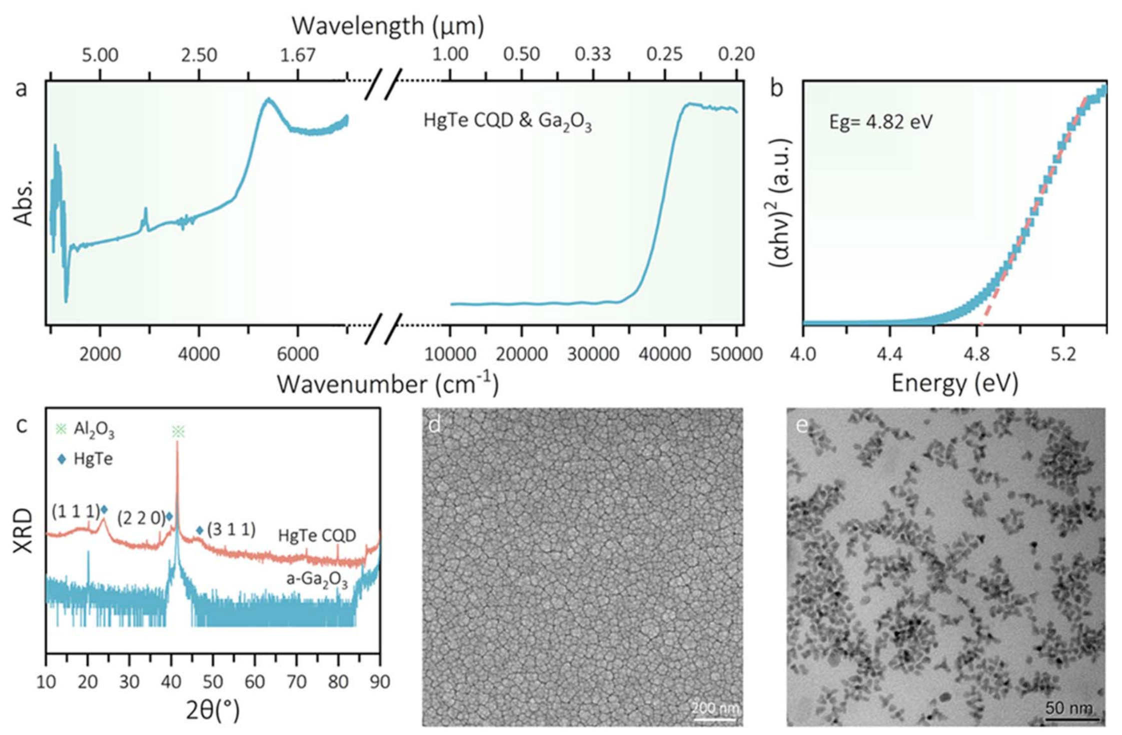

Fig. 1 Material characterization. (a) Absorption spectra of a-Ga_2O_3 and HgTe CQDs; (b) optical bandgap of a-Ga_2O_3 thin film; (c) XRD of a-Ga_2O_3 thin film and HgTe CQDs; (d) SEM images of a-Ga_2O_3; (e) TEM images of HgTe CQDs.

various distances. All characterizations and tests were conducted under ambient room temperature conditions.

3. Results and discussion

Ga_2O_3 SBPD and HgTe CQD photoconductive devices were combined parallelly to achieve dual-band photodetection. Among them, the cutoff wavelengths of the Ga_2O_3 thin film and HgTe CQD film are approximately 40 000 cm^{-1} and 5000 cm^{-1}, respectively, as shown in Fig. 1a, allowing for dual absorption in the solar-blind UV and short-wave infrared regions. To evaluate the optical band gap (E_g) of the Ga_2O_3 film, $(\alpha h\nu)^2$ was plotted with $h\nu$[11] to produce a Tauc plot of the sample (Fig. 1b). The predicted optical band gap of Ga_2O_3 is 4.82 eV. Additionally, no characteristic diffraction peaks associated with the structure of the Ga_2O_3 crystal phase are detected (Fig. 1c), showing that the Ga_2O_3 film is an amorphous phase (a-Ga_2O_3).[24] On the other hand, diffraction peaks are identified at 23.7°, 39.82°, and 46.74° for the HgTe CQD film (Fig. 1d), corresponding to the (1 1 1), (2 2 0), and (3 1 1) planes, respectively.[25] Fig. 1d shows the scanning electron microscope (SEM) images of the samples, demonstrating the smooth surface of the Ga_2O_3 film and the uniform distribution of grain sizes. Fig. 1e shows the transmission electron microscopy (TEM) image of HgTe colloidal quantum dots (CQDs), revealing that the quantum dot size is approximately less than 10 nm.

Ga_2O_3-based photodetectors with ITO as the interdigital electrode have an effective photosensitive area of 0.234 mm^2 with electrode dimensions of 30 μm (spacing and width) and 1 mm (length) under specific incident light irradiation, and hence the resistance of the semiconductor material will change accordingly, and the optoelectronic performance of the device mainly depends on the photoresistive properties of the semiconductor material.[26,27] Thus, under various light intensities, the *I–V* characteristics of the solar-blind DUV photodetector based on a totally transparent a-Ga_2O_3 film were evaluated (Fig. 2a). The photocurrent of the device progressively increases from 21 μA to 67 μA as the light intensity is increased from 5 to 500 μW cm^{-2} with 10 V bias and 254 nm, demonstrating a notable photoresponse to 254 nm UVC light. The linearity of the *I–V* curves from −0.1 to 0.1 V (Fig. S1†) indicates that the ITO electrode and the a-Ga_2O_3 film have good ohmic contact.[28]

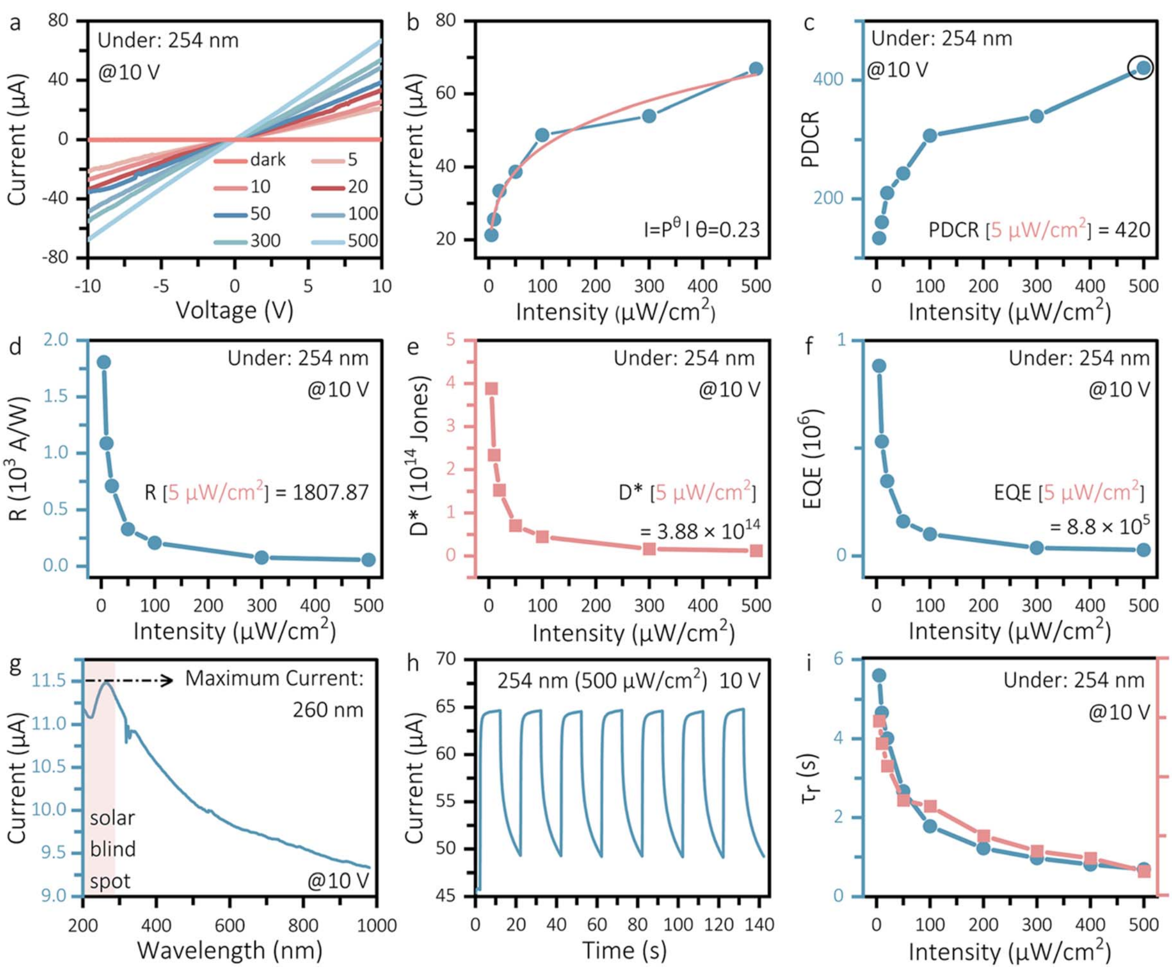

Fig. 2 Optoelectronic properties of the a-Ga_2O_3 SBPD. (a) *I–V* characteristic curves of the a-Ga_2O_3 film-based SBPD; (b) photocurrent and fitting curve; (c) photo-to-dark current ratio; (d) responsivity; (e) detectivity and (f) EQE *versus* light intensity; (g) wavelength-dependent photocurrent curve of the device at a bias voltage of 10 V; (h) transient light response curve at 500 μW cm^{-2} and 10 V bias; (i) response time of the device under 254 nm with different light intensities.

Furthermore, through the power law relationship[29] $I = \alpha P^{\theta}$, where α is a constant, P is the incident optical power, and θ is an exponent representing the dependence of the device on the incident optical power, the fit shows that there is a dependence of the exponent $\theta = 0.23$ between the photocurrent change and the optical intensity (as shown in Fig. 2b), which is a large deviation from the ideal value ($\theta = 1$), which is thought to be due to the fact that the a-Ga_2O_3 film has a number of defects, which affect carrier transport and increase carrier energy loss.[30]

To quantitatively compare the performance of SBPDs based on a-Ga_2O_3 thin films under different 254 nm light intensities, we performed a thorough analysis of several key parameters, including photo-dark current ratio (PDCR), responsivity (R), detectivity (D^*), external quantum efficiency (EQE), and device stability. Among these, the photo-dark current ratio

$$\text{PDCR} = I_p/I_d \quad (1)$$

can approximate the photodetector's signal-to-noise ratio,[31] and Fig. 2c shows the device's growing PDCR as the light intensity increases at a 10 V bias. This matches the changing pattern of photocurrent with intensity, which shows that increasing the unit light flux promotes the creation of electron–hole pairs in semiconductor materials.[28] Furthermore, responsivity (R) is defined as the photocurrent generated per unit power of incident light over an effective area, reflecting a photodetector's ability to convert light energy into electrical energy;[32] D^* is related to noise equivalent power, which evaluates a device's ability to detect weak signals in noisy environments;[33] and EQE is defined as the ratio of electrons–holes to incident photons. The mathematical expressions of these parameters are as follows:[34–39]

$$R = I_p/(S \times P) \quad (2)$$

$$D^* = \left(R \times \sqrt{S}\right) \Big/ \sqrt{(2eI_d)} \quad (3)$$

$$\text{EQE} = hcR/e\lambda \quad (4)$$

where I_p, I_d, S, h, e, λ, and P represent the photocurrent, dark current, effective light area, Planck's constant, electron charge, incident light wavelength, and irradiation intensity, respectively. Fig. 2d–f demonstrates that the SBPD's performance decreases with increasing light intensity, with the optimum R, D^*, and EQE at 5 μW cm^{-2} light being 1808 A W^{-1}, 3.88 × 10^{14} Jones and 8.8 × 10^5%, respectively.

To better understand the photoelectric properties of the a-Ga_2O_3 solar-blind UV detector, the photocurrent curves of the SBPD at different wavelengths at 10 V were examined (Fig. 2g), and the device's photocurrent increases and then decreases as the wavelength increases, with a peak at 260 nm. This means that the device has excellent solar-blind UV sensitivity and spectral selectivity. Repeatability and stability are also crucial characteristics of the solar-blind UV photodetector. To assess device stability, transient photoresponse curves were plotted at 10 V bias and 254 nm (500 μW cm^{-2}) with a 10 second switching cycle, as illustrated in Fig. 2h. The amplitude of the device's photocurrent remains constant after numerous switching cycles, demonstrating that the SBPD is highly stable and reproducible. Fig. S2† depicts the devices' time-dependent photoresponse curves (I–t curves) at 10 V bias voltage and varying light intensities. Under

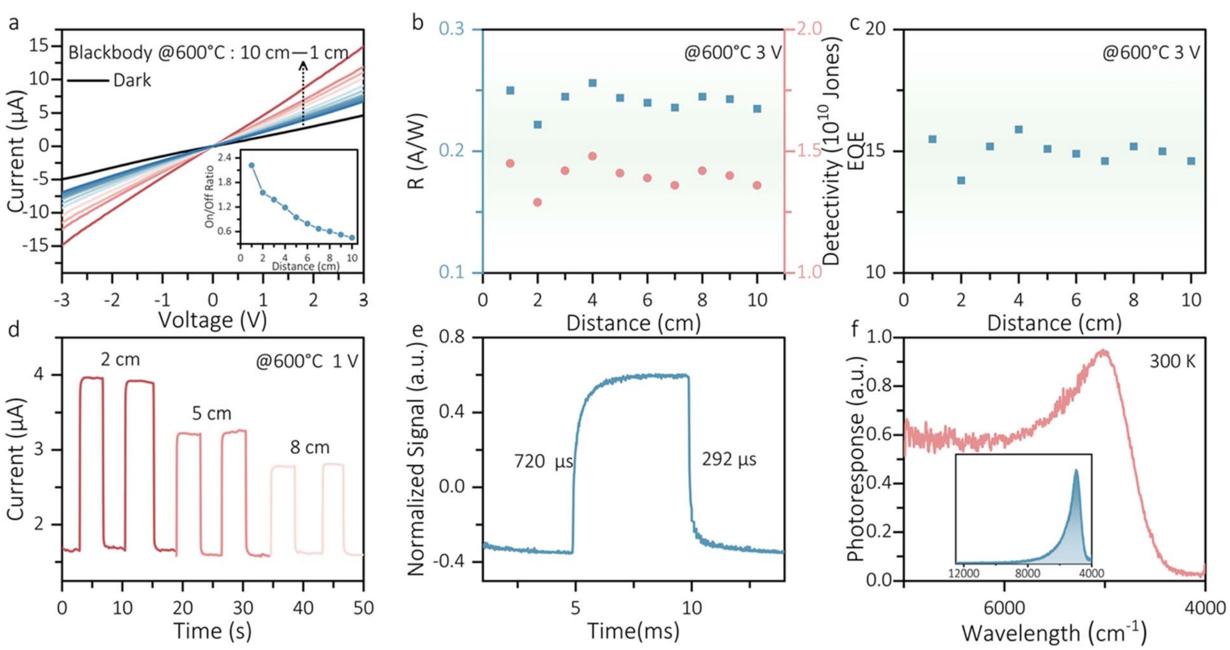

Fig. 3 HgTe CQD photodetector. (a) Current density–voltage curves and on/off ratio (inset graph) of the HgTe CQD photoconductor at different distances from the blackbody; (b) responsivity and detectivity and EQE (c) of the HgTe CQD photoconductor; (d) time-dependent light response curve of the device with different distances; (e) response speed; (f) response spectra normalized with DTGS and as-measured spectral response (inset graph) of the HgTe CQD photoconductor at 300 K.

254 nm light switching, the device shows an apparent photoresponse feature in which increased light intensity stimulates the creation of more photogenerated carriers in the photosensitive layer, resulting in a rise in photocurrent.[40] Additionally, the response speed is a significant factor that characterizes the PD's performance when exposed to transitory light. The photocurrent rises and falls corresponding to the light applied to and removed from the device. The rise time (τ_r) is the period from 10% to 90% of the maximum photocurrent, whereas the fall time (τ_d) is from 90% to 10% of the maximum photocurrent.[41,42] Fig. 2i depicts the relationship between response speed and light intensity at a fixed bias voltage. The Ga_2O_3 material exhibits an inverse trend in response speed as the light intensity increases, with the device's τ_r/τ_d decreasing from 5.6/7.47 s to 0.69/6.2 s, due to the presence of oxygen vacancies and dislocations, which act as trap states.[43]

The dual-band photodetector not only performs well in the solar-blind band, but it also exhibits good optical response in the SWIR range. The *I–V* curves of the HgTe CQD detector at various distances were measured under a 600 °C blackbody light source, as illustrated in Fig. 3a. As the distance increases, the optical power gradually drops, increasing device resistance and producing fewer photogenerated carriers, resulting in a decreased photocurrent.[44] Besides, the photoconductor has the highest on/off ratio (photocurrent/dark current ratio) of 2.22 when it is closest to the blackbody.

We also estimated *R*, EQE and *D** with the conductor area $S = 0.5\ \text{mm}^2$ using eqn (2)–(4), as shown in Fig. 3b and c. The HgTe CQD detector demonstrated a *R*, EQE and *D** of 0.25 A W^{-1}, 15.5% and 1.45×10^{10} at 3 V bias, respectively. Fig. 3d shows the time-dependent photoresponse curves (*I–t* curves) of the devices at 1 V bias voltage with various distances, demonstrating a clear photoresponse signature. The device's response speed was characterized, showing a τ_r/τ_d of 720/292 μs (Fig. 3e). Fig. 3f displays the response spectra at 300 K before and after normalization with DTGS. The HgTe CQD photoconductor has a photoresponse of 2.0 μm (5000 cm^{-1}).

Corona discharges can damage components, resulting in transmission system failures, fires, and other unexpected hazards.[45] If the detector can detect signals such as electromagnetic radiation created during corona discharge consistently, effectively, and precisely, it can assist tiny and simple detectors in inspecting and maintaining high-voltage

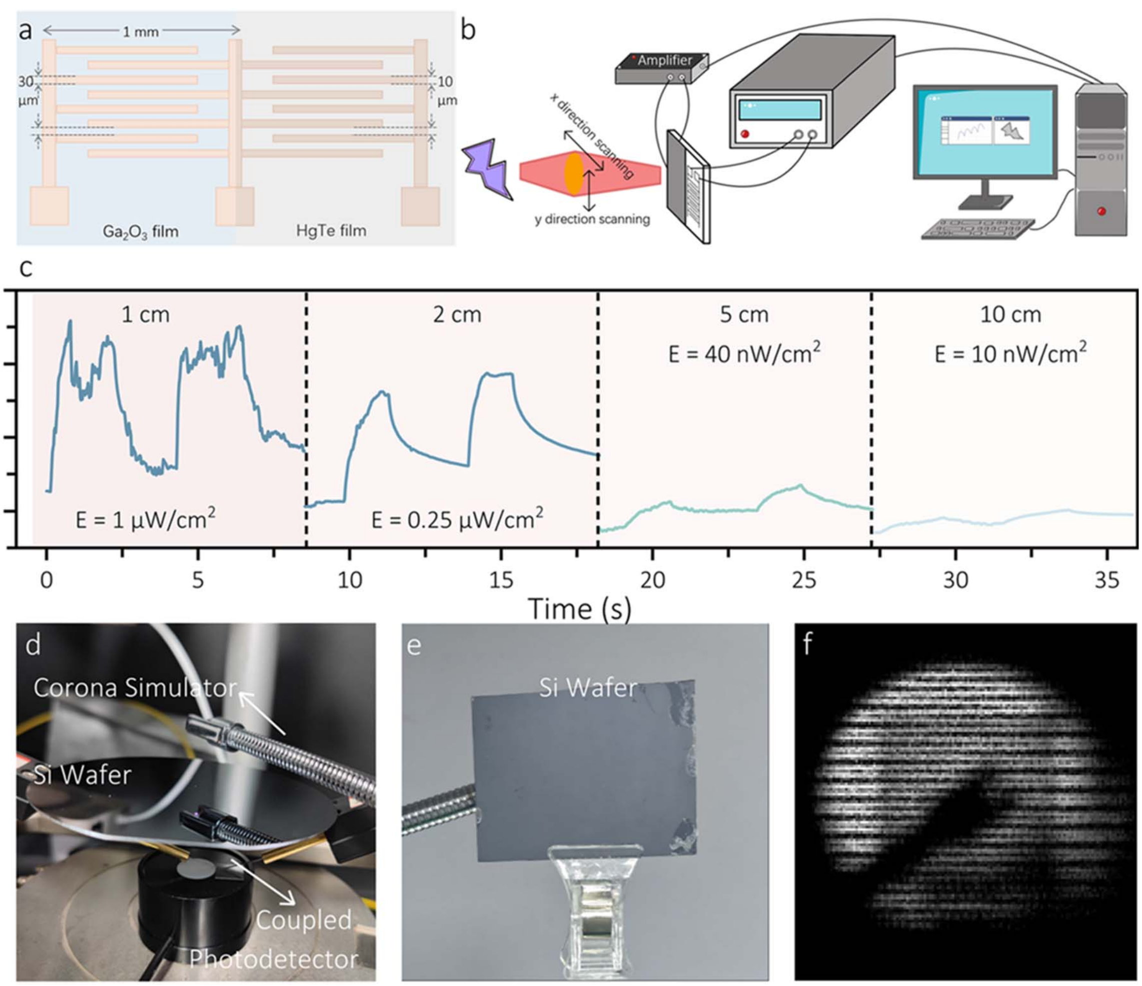

Fig. 4 Dual-band coupled photodetector for corona detection. (a) Schematic of the coupled photoconductor; (b) schematic of the detection process; (c) corona discharge detection results at different distances; (d) corona detection by the SBPD under Si wafer; visible (e) and SWIR (f) images of the arc simulator.

transmission lines from a safety standpoint. The corona detection system in this study is optimized utilizing a dual-band coupled optoelectronic device. Magnetron sputtering and spin-coating on an Al_2O_3 substrate resulted in coupled devices comprising the HgTe CQD photoconductor and a-Ga_2O_3 thin film-based SBPD, and the schematic diagram is shown in Fig. 4a. Fig. 4b displays a model of corona detection using a dual-band photodetector. The arc simulator is employed as a corona source in a high-voltage discharge simulation system because its spectrum corresponds to the high-voltage arc standard spectrum.[46] The system identifies the device's UV and IR detecting capabilities for corona. When it comes to UV detection, the device is tested using a Keithley 2450 for corona discharge detection at various distances. The arc simulator is regarded as a point light source because of its adequately small power generation area, and the incident light intensity E that is irradiated on the a-Ga_2O_3 SBPD can be expressed as[47]

$$E = P_{\text{light}}/(d_{\text{LED}})^2, \quad (5)$$

where d_{LED} is the distance between the arc simulator and the SBPD while P_{light} can be roughly 1 μW by fitting.[24] The test results are displayed in Fig. 4c. The device has an outstanding photoresponse to the high-voltage corona, and the photocurrent signal drops with increasing test distance, and the final detectable limit distance reaches 10 cm while the incident light intensity is 10 nW cm^{-2}. Interestingly, the photon number can be calculated by[48]

$$N = \lambda P_l/hc \quad (6)$$

(in Fig. S3†), where c is the speed of light ($c = 3 \times 10^8$), and P_l is the UV power irradiated on the a-Ga_2O_3 SBPD, expressed as[49]

$$P_l = (P_{\text{light}} \times S)/(d_{\text{LED}})^2. \quad (7)$$

As the distance between the simulator and the SBPD rises, the quantity of photons drops, and at a distance of 10 cm, the number of photons is roughly 3×10^7 photons per s.

In practice, considering that corona detection can be significantly influenced by environmental factors, particularly when electromagnetic signal propagation is blocked, as in Fig. 4d, an opaque silicon wafer is used to block the signal released by the corona simulator, and the device at this point no longer has any photoresponse to the high-voltage corona, as shown in Fig. S4,† implying that the UV detection capability is completely eliminated. Instead, the reflected light of the object from the external light (such as a tungsten lamp or sunlight) is projected onto the CQD device through the lens. The opaque silicon wafer in the visible image is found to be transparent in the SWIR region as shown in Fig. 4e and f. This is an effective solution to the problem of missed detection owing to barriers between the detector and the high voltage line, and it is anticipated to be one of the options for corona discharge detection in the future.

4. Conclusions

In this study, we coupled a HgTe CQD photoconductive device and an a-Ga_2O_3 SBPD to fabricate photodetectors with dual-band detection capability. At a light intensity of 5 μW cm^{-2}, the constructed SBPD had an ultra-high responsivity of 1808 A W^{-1}, and D^* and EQE were up to 3.88×10^{14} and 8.8×10^5%, respectively. The HgTe CQD photoconductor achieved a detectivity of 1.45×10^{10} and a response time of 720/292 μs. Furthermore, we used the dual-band coupled optoelectronic device in corona detection and demonstrated high-voltage corona detection.

Data availability

Data will be made available on request.

Author contributions

All authors commented on the manuscript. All authors have given approval to the final version of the manuscript. Q. Z. finished the photodetector fabrication and characterization as well as drafting the manuscript, and J. Y. assisted in the characterization of the photodetectors. Y. Y., L. L. and A. X. finished data analysis. K. Z. and X. X. finished the CQD synthesis. L. M. finished imaging experiment. W. L. and M. C. worked on conceptualization, study design and data analysis.

Conflicts of interest

The authors declare no competing financial interests.

Acknowledgements

This work is supported by Optoelectronic Measurement and Intelligent Perception Zhongguancun Open Lab LabSOMP-2024-01, National Natural Science Foundation of China (No. 62475012); State Key Laboratory of Materials for Integrated Circuits (No. SKLJC-K2024-07); Beijing National Laboratory for Condensed Matter Physics (No. 2023BNLCMPKF012); and Westlake Institute for Optoelectronics (No. 2024GD003).

References

1 D. Lee, S. Jeong, S. Moon, M. Yang, S. Kim, D. Kim, S. Lee, I. Lee, D. Jeon, J. Park, J. Kim and S. Baek, *ACS Nano*, 2024, **18**(51), 34741–34749.
2 G. Ariyawansa, M. B. M. Rinzan, M. Alevli, M. Strassburg, N. Dietz, A. G. U. Perera, S. G. Matsik, A. Asghak, I. T. Ferguson, H. Luo, A. Bezinger and H. C. Liu, *Appl. Phys. Lett.*, 2006, **89**, 9.
3 J. He, X. S. Xing, X. B. Song, S. Y. Li, C. Zhang and W. Wang, *Proceedings of the 3rd ICITEE*, 2020, pp. 202–207.
4 W. Zheng, R. Lin, J. X. Ran, Z. J. Zhang, X. Ji and F. Huang, *ACS Nano*, 2018, **12**, 425–431.

5 C. H. Zeng, W. K. Lin, Y. H. Sun, Q. Cui, X. Zhang, S. J. Li, B. S. Zhang and M. Kong, *Optoelectronics Letters*, 2019, **15**, 170–173.
6 Z. F. Zhang, C. N. Lin, X. Yang, J. H. Zang, K. Y. Li, Y. C. Lu, Y. Z. Li, L. Dong and C. X. Shan, *J. Mater. Chem. C*, 2022, **10**, 6488–6496.
7 M. R. Chen, S. H. Chang, T. C. Chen, C. H. Hsu, H. L. Kao and J. I. Chyi, *Phys. Status Solidi A*, 2010, **207**, 224–228.
8 J. H. Kim, C. Y. Han, K. H. Lee, K. S. An, W. Song, J. Kim, M. S. Oh, Y. R. Do and H. Yang, *Chem. Mater.*, 2015, **27**, 197–204.
9 Y. Qin, L. H. Li, Z. Yu, F. Wu, D. Dong, W. Guo, Z. F. Zhang, J. H. Yuan, K. H. Xue, X. S. Miao and S. B. Long, *Adv. Sci.*, 2021, **8**, 2101106.
10 C. Xie, X. Lu, Y. Liang, H. Chen, L. Wang, C. Wu, W. H. Yang and L. B. Luo, *J. Mater. Sci. Technol.*, 2021, **72**, 189–196.
11 S. R. Zhou, Q. Q. Zheng, C. X. Yu, Z. H. Huang, L. R. Chen, H. Zhang, H. L. Li, Y. Q. Xiong, C. Y. Kong, L. J. Ye and W. J. Li, *Mater*, 2022, **16**, 295.
12 H. Yang, Y. Liu, X. G. Luo, Y. Li, D. S. Wuu, K. Y. He and Z. C. Feng, *Superlattices Microstruct.*, 2019, **131**, 21–29.
13 W. Y. Kong, G. A. Wu, K. Y. Wang, T. F. Zhang, Y. F. Zou, D. D. Wang and L. B. Luo, *Adv. Mater.*, 2016, **28**, 10725–10731.
14 A. Almalki, L. Madani, N. Sengouga, S. Alhassan, S. Alotaibi, A. Alhassni, A. Almunyif, J. S. Chauhan, M. Henini, H. V. A. Galeti, Y. G. Gobato, M. P. F. Godoy, M. B. Andrade, S. Souto, H. Zhou, B. Y. Wang, M. Xiao, Y. Qin and Y. H. Zhang, *Mater. Today Electron.*, 2023, **4**, 100042.
15 T. He, C. Li, X. Zhang, Y. J. Ma, X. Cao, X. Y. Shi, C. Shi, J. S. Li, L. Song, C. H. Zeng, K. Zhang, X. P. Zhang and B. S. Zhang, *Phys. Status Solidi A*, 2020, **217**, 1900861.
16 T. Chen, J. R. Zhang, X. D. Zhang, C. Chen, L. Zhang and Y. Hu, *IEEE Sens. J.*, 2023, **23**, 15504–15511.
17 X. Zhao, X. Tang, T. P. Li and M. L. Chen, *Infrared Phys. Technol.*, 2023, **133**, 104788.
18 S. G. Kumar and K. K. Rao, *Energy Environ. Sci.*, 2014, **7**, 45–102.
19 X. M. Xue, M. L. Chen, Y. N. Luo, T. L. Qin, X. Tang and Q. Hao, *Light: Sci. Appl.*, 2023, **12**, 2.
20 Y. Luo, S. Zhang, X. Tang and M. L. Chen, *J. Mater. Chem. C*, 2022, **10**, 8218–8225.
21 X. M. Xue, Q. Hao and M. L. Chen, *Light: Sci. Appl.*, 2024, **13**, 89.
22 Y. Y. Qiu, N. Q. Yan, H. F. Yao and M. L. Chen, *Infrared Phys. Technol.*, 2023, **135**, 104980.
23 S. Zhang, C. Bi, Y. M. Tan, Y. N. Luo, Y. F. Liu, J. Cao, M. L. Chen, Q. Hao and X. Tang, *ACS Nano*, 2022, **16**, 18822–18829.
24 X. D. Li, F. Y. Xu, X. Wang, J. S. Luo, K. Ding, L. Y. Ye, H. L. Li, Y. Q. Xiong, P. Yu, C. Y. Kong, L. J. Ye, H. Zhang and W. J. Li, *Phys. Status Solidi RRL*, 2024, **18**, 2200512.
25 Z. K. Liu, P. Wang, R. Dong, W. Gong, J. J. Li, D. C. Dai, H. Yan and Y. Z. Zhang, *Coatings*, 2022, **12**, 1033.
26 J. Bae, D. W. Jeon, J. H. Park and J. Kim, *J. Vac. Sci. Technol., A*, 2021, **39**, 033410.
27 H. T. Zhou, L. J. Cong, J. G. Ma, B. S. Li, M. Z. Chen, H. Y. Xu and Y. C. Liu, *J. Mater. Chem. C*, 2019, **7**, 13149–13155.
28 Z. H. Huang, S. R. Zhou, L. R. Chen, Q. Q. Zheng, H. L. Li, Y. Q. Xiong, L. J. Ye, C. Y. Kong, S. Q. Fan, H. Zhang and W. J. Li, *Crystals*, 2022, **12**, 1427.
29 S. R. Zhou, H. Zhang, X. Peng, H. W. Liu, H. L. Li, Y. Q. Xiong, W. J. Li, P. A. Yang, L. J. Ye and C. Y. Kong, *Adv. Photonics Res.*, 2022, **3**, 2202192.
30 L. Wang, J. S. Jie, Z. B. Shao, Q. Zhang, X. H. Zhang, Y. M. Wang, S. Zheng and S. Lee, *Adv. Funct. Mater.*, 2015, **25**, 2910–2919.
31 Y. Qin, L. H. Li, X. L. Zhao, G. S. Tompa, H. Dong, G. Z. Jian, Q. M. He, P. J. Tan, X. H. Hou, Z. F. Zhang, S. J. Yu, H. D. Sun, G. W. Xu, X. S. Miao, K. H. Xue, S. B. Long and M. Liu, *ACS Photonics*, 2020, **7**, 812–820.
32 J. Wang, Y. Q. Xiong, L. J. Ye, W. J. Li, G. P. Qin, H. B. Ruan, H. Zhang, L. Fang, C. Y. Kong and H. L. Li, *Opt. Mater.*, 2021, **112**, 110808.
33 C. T. Wei, J. P. Xu, S. B. Shi, R. Cao, J. Chen, H. Dong, X. S. Zhang, S. G. Yin and L. Li, *J. Mater. Chem. C*, 2019, **7**, 9369–9379.
34 Q. Q. Zheng, L. R. Chen, X. D. Li, K. Ding, D. Pang, H. L. Li, Y. Q. Xiong, H. B. Ruan, L. Fang, W. J. Li, L. J. Ye, H. Zhang and C. Y. Kong, *Sci. China: Technol. Sci.*, 2023, **66**, 2707–2715.
35 K. H. Li, X. K. Yang, F. F. Yang, J. G. He, G. Z. Zhang, S. L. Jiang, C. Chen and J. Tang, *Mater. Today Electron.*, 2022, **2**, 100011.
36 X. C. Liang, C. Hou, Z. H. Wu, Z. T. Wu and G. A. Tai, *Nanotechnology*, 2023, **34**, 205701.
37 Z. H. Wu, C. Shifan, Z. T. Wu, Y. Liu, W. Shao, X. C. Liang, C. Hou and G. A. Tai, *Nano Res.*, 2024, **17**, 3053–3060.
38 Y. Liu, G. A. Tai, C. Hou, Z. T. Wu and X. C. Liang, *ACS Appl. Mater. Interfaces*, 2023, **15**, 14566–14574.
39 G. A. Tai, B. Liu, C. Hou, Z. T. Wu and X. C. Liang, *Nanotechnology*, 2021, **32**, 505606.
40 S. Oh, C. K. Kim and J. Kim, *ACS Photonics*, 2017, **5**, 1123–1128.
41 L. Chen, B. Y. Wang, J. Q. Dong, F. L. Gao, H. W. Zheng, M. He and X. F. Wang, *Nano Energy*, 2020, **78**, 105260.
42 Y. L. Yu, Y. Hu, J. H. Yang and Z. M. Wei, *Mater. Today Electron.*, 2022, **2**, 100013.
43 Y. H. Wang, S. Y. Li, J. Cao, Y. C. Jiang, Y. Zhang, W. H. Tang and Z. P. Wu, *Mater. Des.*, 2022, **221**, 110917.
44 X. M. Xue, Y. N. Luo, Q. Hao, J. Cao, X. Tang, Y. F. Liu and M. L. Chen, *ACS Photonics*, 2023, **10**, 4290–4298.
45 M. M. Yaacob, M. A. Alsaedi, J. R. Rashed, A. M. Dakhil and S. F. Atyah, *Photonic Sens.*, 2014, **4**, 325–337.
46 H. W. Liu, S. R. Zhou, H. Zhang, L. J. Ye, Y. Q. Xiong, P. Yu, W. J. Li, X. Yang, H. L. Li and K. C. Yang, *J. Phys. D: Appl. Phys.*, 2022, **55**, 305104.
47 Y. Q. Yu, L. B. Luo, M. Z. Wang, B. Wang, L. H. Zeng, C. Y. Wu, J. S. Jie, J. W. Liu, L. Wang and S. H. Yu, *Nano Res.*, 2015, **8**, 1098–1107.
48 M. Rabia, A. M. Elsayed and M. A. Alnuwaiser, *Micromachines*, 2023, **14**, 1573.
49 Y. Q. Yu, L. B. Luo, M. Z. Wang, B. Wang, L. H. Zeng, C. Y. Wu, J. S. Jie, J. W. Liu, L. Wang and S. H. Yu, *Nano Res.*, 2015, **8**, 1098–1107.

